










## Direct measurement of $^{59}\text{Ni}(n, p)^{59}\text{Co}$ and $^{59}\text{Ni}(n, \alpha)^{56}\text{Fe}$ at fast-neutron energies from 500 keV to 10 MeV

S. A. Kuvin <sup>\*</sup>, H. Y. Lee , B. DiGiovine , C. Eiroa-Lledo, A. Georgiadou, M. Herman , T. Kawano , V. Mocko ,  
S. Mosby, C. Vermeulen , D. Votaw , M. White , and L. Zavorka<sup>†</sup>  
*Los Alamos National Laboratory, Los Alamos, New Mexico 87545, USA*

G. Perdikakis  and P. Tsintari

*Department of Physics, Central Michigan University, Mount Pleasant, Michigan 48859, USA*

H. I. Kim 

*Nuclear Physics Application Research Division, Korean Atomic Energy Research Institute, Yuseong-gu, Daejeon, Korea*



(Received 10 February 2022; accepted 11 March 2022; published 11 April 2022)

Nuclear reaction data for neutron induced reactions on unstable nuclei are critical for a wide range of applications spanning studies of nuclear astrophysics, nuclear reactor designs, and radiochemistry diagnostics. However, nuclear data evaluations of the reaction cross sections are largely based on calculations due to the difficulty in performing this class of measurements and the resulting lack of experimental data. For neutron induced charged particle reactions at fast neutron energies, at the MeV scale, these cross section predictions are predominately driven by statistical Hauser-Feshbach calculations. In this work, we present partial and total  $^{59}\text{Ni}(n, p)$  and  $^{59}\text{Ni}(n, \alpha)$  cross sections, measured directly with a radioactive  $^{59}\text{Ni}$  target, and compare the results to the present nuclear data evaluations. In addition, the results from this work are compared to a recent study of the  $^{59}\text{Ni}(n, xp)$  reaction cross section that was performed via an indirect surrogate ratio method. The expected energy trend of the cross section, based on the current work, is inconsistent with that of the surrogate work. This calls into question the reliability of that application of the surrogate ratio method and highlights the need for direct measurements on unstable nuclei, when feasible.

DOI: [10.1103/PhysRevC.105.044608](https://doi.org/10.1103/PhysRevC.105.044608)

### I. INTRODUCTION

Improved experimental data for neutron induced charged particle reactions on the isotopes of iron, chromium, and nickel are important for characterizing phenomena like embrittlement and the damage caused by hydrogen and helium production in structural materials [1]. A significant amount of  $^{59}\text{Ni}$ , although not a naturally occurring isotope of nickel, is produced in reactors from neutron capture on  $^{58}\text{Ni}$  at thermal energies and from  $^{60}\text{Ni}(n, 2n)$  at fast-neutron energies in fusion reactors. Since  $^{59}\text{Ni}$  has a very long half-life ( $T_{1/2} \approx 100\,000$  years), it can build up to a significant portion ( $>4\%$ ) of the total nickel content [2]. At this point ( $n, p$ ) and ( $n, \alpha$ ) reactions on  $^{59}\text{Ni}$  can be a significant driver of energy production due to the large positive  $Q$  values for these reactions and the large cross sections at thermal energies [3,4]. In this work, we present energy- and angle-integrated partial and total cross sections for  $^{59}\text{Ni}(n, p)$  and  $^{59}\text{Ni}(n, \alpha)$  reactions at fast-neutron energies up to 10 MeV. In combination with experimental data on the stable nickel isotopes, this information will be used to help provide a more complete evaluation of all the nickel isotopes that will also include a recent measurement on the short-lived  $^{56}\text{Ni}$  radioisotope.

For the measurement of neutron-induced reactions on short-lived  $^{56}\text{Ni}$ , a radioactive target was produced at the Isotope Production Facility at the Los Alamos Neutron Science Center (LANSCE), purified and fabricated at the Isotope Program Hot Cell Facility, and then studied using the fast-neutron beams available at the Weapons Neutron Research (WNR) facility, also at LANSCE [5]. However, the production of  $^{56}\text{Ni}$  via  $^{59}\text{Co}(p, xn)$  reactions also results in the production of  $^{57}\text{Ni}$ ,  $^{58}\text{Ni}$ , and  $^{59}\text{Ni}$  that will all be present in the final radioactive cocktail target, without performing further mass separation. Since  $^{56}\text{Ni}$  and  $^{57}\text{Ni}$  will decay swiftly with day-long half-lives, whereas  $^{58}\text{Ni}$  (stable) and  $^{59}\text{Ni}$  (long lived) will not, the charged particle backgrounds due to  $^{58}\text{Ni}(n, z)$  and  $^{59}\text{Ni}(n, z)$  will be dominant. Measurements of the stable nickel isotopes are captured in many past measurements [6], and have also recently been measured at LANSCE with an experimental setup consistent with this work. However, the lack of past experimental data on  $^{59}\text{Ni}(n, p)$  or  $^{59}\text{Ni}(n, \alpha)$  at fast-neutron energies above 100 keV presents a technical consideration for the study of  $^{56}\text{Ni}(n, p)$  that needs to be characterized.

Although  $^{59}\text{Ni}$  is a long-lived radioisotope of nickel, it is bookended by the stable  $A = 58$  and  $A = 60$  isotopes. Naively, one would expect that the evaluations of the stable isotopes to be relatively well constrained at this point, and that this constraint would extend to predictions of the  $^{59}\text{Ni} + n$

<sup>\*</sup>kuvin@lanl.gov

<sup>†</sup>Current address: Oak Ridge National Laboratory.

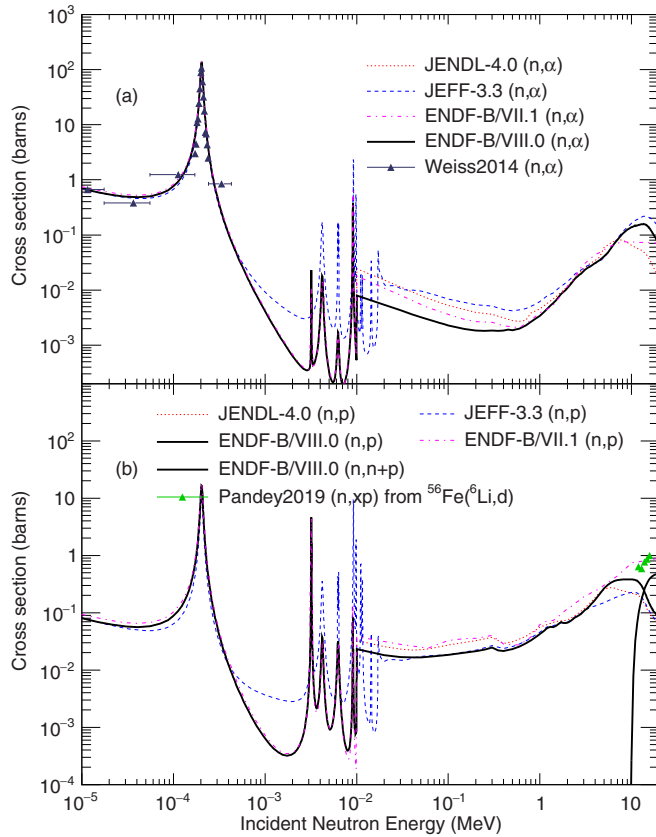


FIG. 1. The current status of  $^{59}\text{Ni}(n, p)$  (bottom panel) and  $^{59}\text{Ni}(n, \alpha)$  (top panel) cross sections are shown in comparison to evaluated data libraries [7–9] and a limited selection of experimental data [12,18]. At fast-neutron energies, for which there are no experimental data available from studying the reactions directly, the evaluations are very discrepant.

system. However, as shown in both panels of Fig. 1, there is significant variation between the evaluations [7–9] of  $(n, p)$  and  $(n, \alpha)$  at neutron energies above the dominant resonance at 200 eV. This resonance has been studied at the Oak Ridge Electron Linear Accelerator (ORELA) [10,11] and the neutron time-of-flight facility at CERN (n\_TOF) [12] and there have also been a few measurements of  $(n, \alpha)$  near thermal energies [10,13,14]. Meanwhile, the work of Harvey *et al.* [10] measured resonance parameters in  $(n, p)$  and  $(n, \alpha)$  up to approximately 20 keV. Due to the lack of experimental data at higher energies, the evaluations are guided by the limited available reaction data on  $^{59}\text{Ni}(n, \text{total})$  that is available up to approximately 200 keV [10,15] and the statistical calculations [16] above that are informed by the nearby isotopes. In the evaluation of Helgesson *et al.* [17], which is incorporated into the JEFF-3.3 library [9], the uncertainties and covariances at fast-neutron energies were based on randomized input parameters to a set of statistical calculations. Going from the lower edge to the upper edge of the  $\pm 1\sigma$  bounds in that work represents a range that covers nearly a factor of 5 in the  $(n, p)$  cross section at fast-neutron energies.

Most recently, a study by Pandey *et al.* [18] used a surrogate ratio method studying the  $^{56}\text{Fe}(^6\text{Li}, d)$  reaction to

infer the total proton production  $(n, xp)$  cross section on  $^{59}\text{Ni}$  at neutron energies above 10 MeV. Their results were presented in the context of statistical calculations that could not reproduce the magnitude or trend of their experimental cross sections without a significant adjustment to the optical model potential. The adjustment to the calculation that they adopt increases the magnitude of the  $(n, p)$  cross section over the entire neutron energy range such that there is a factor of 3 difference between their calculation and the ENDF/B-VIII.0 library at 2 MeV. In addition, the cross sections that they report are also outside the  $1\sigma$  bounds of the JEFF-3.3 evaluation that was described in the work of Helgesson *et al.* [9,17].

By performing a direct measurement of the  $^{59}\text{Ni}(n, p)$  reaction, along with measurements on other accessible unstable nuclei, we can provide the necessary benchmarks that are needed to inform the reliability of any cross sections results that are derived from calculations or surrogate methods as they are extended further from stability. Until now, these surrogate methods have been explored primarily for determining fission and capture reaction cross sections in actinides; however, there is significant interest in extending the capabilities to a wider range of reaction channels in different mass regimes [19]. At the moment, the literature is lacking in regards to extending the theoretical framework to studies of  $(n, z)$  reactions on intermediate mass nuclei and it is expected that the reliability of the surrogate method will still need to be tested for each isotope on a case-by-case basis [20,21].

## II. EXPERIMENT

### A. Unmoderated neutron source at LANSCE

The measurement of neutron induced charged particle reactions on  $^{59}\text{Ni}$  was performed at the WNR facility at the Los Alamos Neutron Science Center (LANSCE) [5]. The LANSCE accelerator delivers 800 MeV protons to the unmoderated tungsten target at WNR, generating neutrons with a broad energy spectrum via spallation. In this work, measurements were taken at flight path 15R, at a distance of 15.191 m from the center of the spallation target to the target position of our experimental setup.

The time structure of the proton beam consisted of 100 macropulses/second, with each 625  $\mu\text{s}$  long macropulse consisting of approximately 340 micropulses, each separated by 1.8  $\mu\text{s}$ . Depending on the flight path length, the time structure imposes a minimum neutron energy before frame overlap occurs, and the low energy neutrons can no longer be distinguished from the high energy neutrons of the subsequent pulse. For example, at a flight path length of 15 m, the minimum energy that can be resolved is approximately 350 keV. To characterize this frame overlap, two days of beam time was dedicated to operate the accelerator with a micropulse spacing of 3.6  $\mu\text{s}$ , corresponding to a neutron energy frame with a minimum energy just below 100 keV.

### B. Experimental setup

The outgoing charged particles from  $(n, p)$  and  $(n, \alpha)$  reactions were detected using the Low Energy  $(n, z)$  (LENZ) experimental setup [22,23], consisting of annular double-sided

silicon strip detectors. The two S1 detectors [24] were located downstream of the target sample, covering forward laboratory angles ranging 45–65 degrees and 15–30 degrees. The signals from the LENZ detectors and auxiliary monitor detectors were readout using a digital data acquisition system consisting of 16-channel CAEN VX1730 digitizers, as discussed in Ref. [23].

The 95% enriched  $^{59}\text{Ni}$  targets ( $91 \mu\text{g}/\text{cm}^2$ ) were fabricated at ORELA during the 1970s and used in multiple measurements [10–12]. Most recently, the targets were used at n\_TOF at CERN for a measurement of  $^{59}\text{Ni}(n, \alpha)$  using a diamond detector [12]. Due to the long half-life of  $^{59}\text{Ni}$ , no loss of target material is expected. A  $^{59}\text{Ni}$  target with an additional  $104 \mu\text{g}/\text{cm}^2$   $^6\text{LiF}$  deposit was used to check the overall flux normalization via the  $^6\text{Li}(n, t)^4\text{He}$  reaction. In addition, the neutron flux was actively monitored via the  $^{238}\text{U}(n, f)$  reaction with an ionization detector [25] loaded with a  $^{238}\text{U}$  foil throughout the duration of the experiment. The uncertainties for the thicknesses of the electroplated deposits is expected to be <2% and a reasonable estimate of 5% for the uncertainty in the number of  $^{59}\text{Ni}$  target atoms has been adopted. This is based on a past study [14] that was conducted with  $^{59}\text{Ni}$  targets, produced at ORELA, which were contemporary to the target currently under study. The target sample deposits were 1.5 cm in diameter on target frames that were nearly two inches in diameter. To accommodate this target size, the neutron beam was collimated down to approximately 1 cm in diameter. The overall beam time for this experiment was limited to a total of only 12 days, with 1.5 days dedicated to measurement with the Pt backing, 2 days with the LiF target, and a total of 8 days with the  $^{59}\text{Ni}$  target. This includes the two days that were dedicated for characterizing the frame overlap with the longer micropulse spacing. Depending on the availability of future beam time at WNR, additional measurements with detector coverage at both forward and backward angles would help improve the statistical uncertainties from this work and extend the measurements to higher incident neutron energies.

The location of the experimental setup and the end of the beam collimation, relative to the WNR target, were measured by making use of a suite of metrology instruments including LIDAR (light detection and ranging), laser trackers utilizing ADM (absolute distance measurement), and laser scanning via a Creaform MetraSCAN 750 optical CMM (coordinate measuring machine). Recent upgrades to the WNR spallation target included integral retroreflective fiducials which [26] allowed for a precise determination of the flight path length relative to the center of the spallation target by laser tracker ADM measurement. Consistency checks were made by inserting a carbon filter into the upstream collimation to leave an imprint of the  $^{12}\text{C} + n$  resonances into the neutron energy spectrum. The notches in the measured neutron flux at known resonance energies were observed in the  $^{238}\text{U}(n, f)$  spectrum measured with the ionization chamber and in the  $^1\text{H}(n, \text{el})$  proton recoil data, from using a  $\text{CH}_2$  target, measured with the LENZ silicon detectors. As discussed in Ref. [27], a diamond detector was also used to measure the flight path lengths at 15R and 90L by directly measuring the time of flight associated with the  $^{12}\text{C} + n$  resonances.

In addition to the flight path length measurements, the laser scanning tools allowed us to generate a three-dimensional point cloud of the experimental area, including the target, detectors, chamber, and collimation to obtain an as-assembled geometry of the experimental setup and check for the potential misalignment of any elements.

### III. ANALYSIS

#### A. Beam normalization

The shape of the neutron flux from 100 keV to 20 MeV was characterized using a combination of ionization chambers [25] loaded with  $^{238}\text{U}$  and  $^{235}\text{U}$  foils. The overall normalization was obtained using the ionization chamber loaded with  $^{238}\text{U}$  that was monitoring the beam during the duration of this experiment. Validation of the overall normalization was made via measurements of  $^1\text{H}(n, \text{el})$  and  $^6\text{Li}(n, t)$  with the same experimental setup used to measure the  $^{59}\text{Ni}(n, z)$  reactions. Typically, the ionization chambers under use are considered reliable at the 8% level due to potential nonuniformities in the uranium deposit thickness, but here we adopt a 5% uncertainty based on the consistency between the relative measurements.

Since there is no threshold for the  $^6\text{Li}(n, t)$  reaction nor for the  $^{235}\text{U}(n, f)$  reaction, frame overlap begins to occur at around 350 keV with  $1.8 \mu\text{s}$  beam spacing at a flight path length of 15 m. Therefore, the wraparound contribution due to frame overlap is characterized with the experimental data recorded with a  $3.6 \mu\text{s}$  beam spacing that was taken for 2 days. One day was dedicated to the measurement with the  $^6\text{Li}$  deposit, and the second day dedicated to the target with the  $^{59}\text{Ni}$  sample alone.

#### B. Reconstructing the reaction $Q$ value

The reaction  $Q$  value is reconstructed from the detected energy and angle of the outgoing charged particle and from the incident neutron energy that is determined by the time of flight from the spallation target to the silicon detectors. A recoil time of flight correction is applied to account for the finite time of flight of the detected charged particle from the target sample to the detectors, as previously discussed in Sec. III of Ref. [23]. The correlation between the detected charged particle energy and the neutron time-of-flight (with respect to the arrival of the gamma rays), for different target samples and  $1.8 \mu\text{s}$  spacing, is shown in Fig. 2. Different reaction channels are identified by the kinematic curves which correspond to a particular reaction  $Q$  value.

In the top two panels of Fig. 2, the dominant lines at higher detected energy are from the  $^6\text{Li}(n, t)\alpha$  ( $Q$  value = +4.78 MeV) reaction, corresponding to the detection of either the triton or the  $\alpha$  particle. Here, the detection of  $\alpha$  particles at forward angles corresponds to tritons that were emitted at backward c.m. angles. The important feature to note is the events with near constant detected energy that are present at all values of measured time of flight. These events are due to the frame overlap that was previously discussed, corresponding to  $^6\text{Li}(n, t)$  events induced by low energy neutrons that have exceeded the time cutoff of  $1.8 \mu\text{s}$  and thereby interfere with the subsequent micropulse. In comparison, the top two

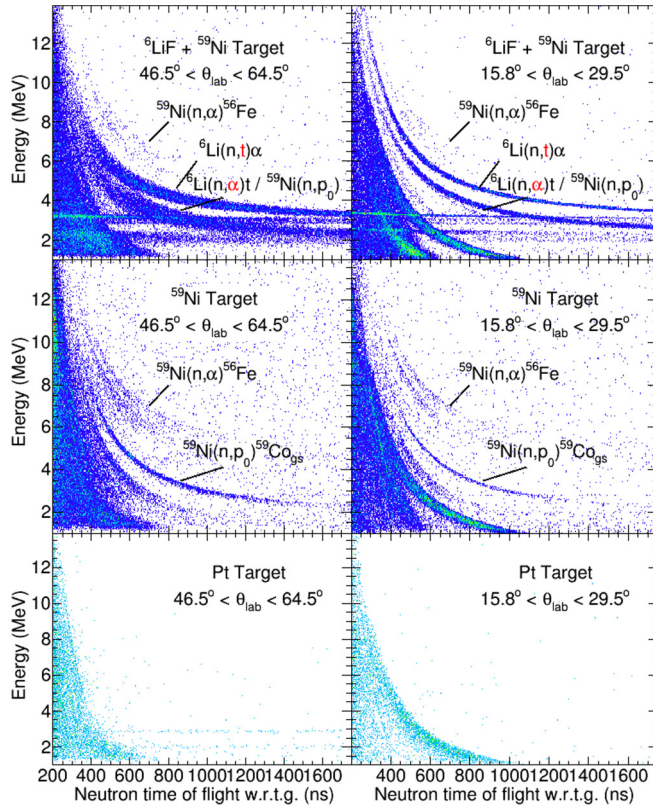


FIG. 2. The correlation between energy and time of flight is used to identify particular reaction channels for the (top panels)  ${}^6\text{LiF} + {}^{59}\text{Ni}$  target, (middle panels) the  ${}^{59}\text{Ni}$  target, and the (bottom panels) Pt background target. The contributions due to frame-overlap, owing to the  $1.8 \mu\text{s}$  LANSCE proton beam pulse-spacing, is most evident in the top panels due to  ${}^6\text{Li}(n,t)\alpha$  reactions occurring at low neutron energies.

panels of Fig. 3, with a micropulse spacing of  $3.6 \mu\text{s}$ , still have this overlap feature but the effect is not as prominent. Regardless, extracting the yield of the triton events in the  $1.8 \mu\text{s}$  data, as shown in Fig. 4, is not affected by this frame overlap, as the lower energy events are not reconstructed with the correct  $Q$  value (due to incorrect identification of the incident neutron energy). Here, the  $Q$  value is reconstructed assuming that the detected particle is a triton and that the missing mass is the  $\alpha$  particle, therefore, the events corresponding to the detection of an  $\alpha$  particle appear at a lower  $Q$  value.

The second set of panels in Figs. 2 and 3 correspond to the  ${}^{59}\text{Ni}$  targets that are without the additional  ${}^6\text{LiF}$  deposits. As a result, we can now clearly identify the  ${}^{59}\text{Ni}(n,p)$  and  ${}^{59}\text{Ni}(n,\alpha)$  reaction channels. Here, we find that the wraparound contribution is a smaller contribution because the  ${}^{59}\text{Ni}(n,p)$  and  ${}^{59}\text{Ni}(n,\alpha)$  cross sections are not increasing as rapidly with decreasing neutron energy, as compared to the  ${}^6\text{Li}(n,t)\alpha$  reaction cross section. Figure 5 shows the reconstructed reaction  $Q$  value, assuming the detected particle was a proton and the missing mass is  ${}^{59}\text{Co}$ . Here, we can clearly identify the contributions from  ${}^{59}\text{Ni}(n,p){}^{59}\text{Co}$  (ground state  $Q$  value =  $+1.85$  MeV) from  ${}^{59}\text{Ni}(n,\alpha){}^{56}\text{Fe}$  (ground state  $Q$  value =  $+5.09$  MeV) through the combination of the

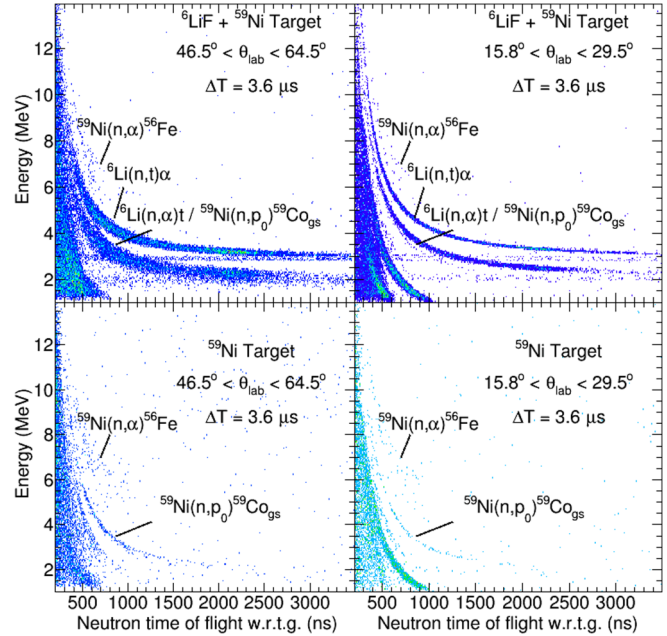


FIG. 3. The correlation between energy and time of flight for the LANSCE proton beam pulse-spacing set to  $3.6 \mu\text{s}$  for the (top panels)  ${}^6\text{LiF} + {}^{59}\text{Ni}$  target and the (bottom panels)  ${}^{59}\text{Ni}$  target.

measured  $Q$  value and the rise-time pulse shape discrimination that is discussed in Sec. III C. In this figure, the  $(n,\alpha)$  events appear shifted down from their nominal  $Q$  values, due to kinematics and a slightly different dead-layer correction,

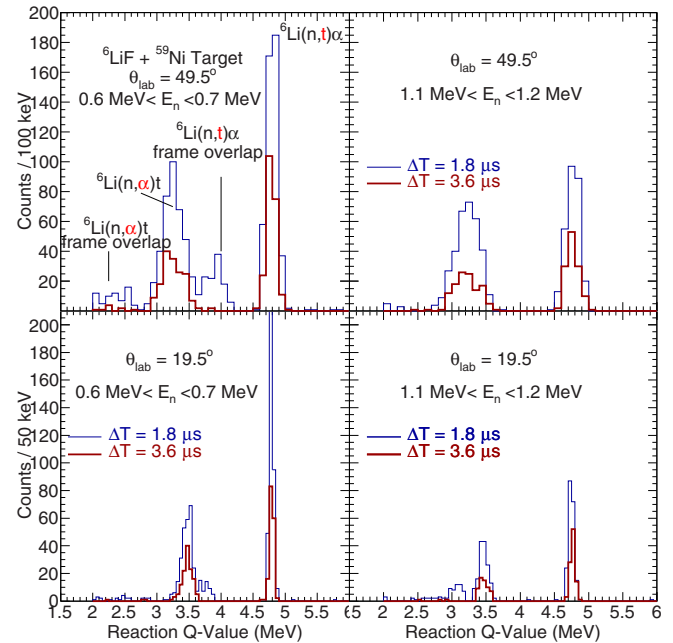


FIG. 4. Projections of the reconstructed reaction  $Q$  value for the  ${}^6\text{Li}$  target, assuming the detection of a triton, at different neutron energy bins (left-right panels) and two different angles (top-bottom panels). The background contributions due to frame overlap are highlighted in the top-left panel.

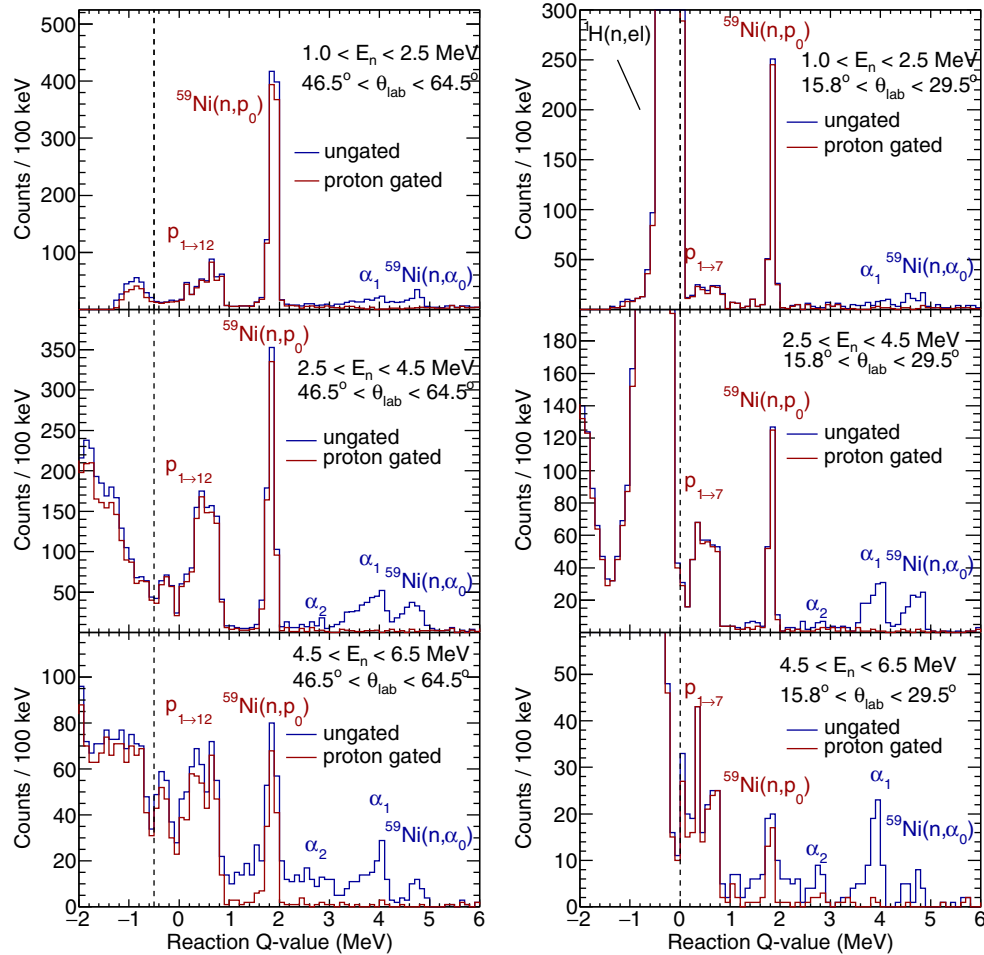


FIG. 5. Projections of the reconstructed reaction  $Q$  value for the  $^{59}\text{Ni}$  target, assuming an outgoing proton and  $^{59}\text{Co}$  residual nucleus, at different neutron energy bins (top-bottom) and angle ranges (left-right). Rise-time pulse shape discrimination is used to discriminate between the  $(n, p)$  and  $(n, \alpha)$  reaction channels as illustrated by the “proton-gated” spectrum. Here the dominant peak at 1.8 MeV is from the  $^{59}\text{Ni}(n, p_0)^{59}\text{Co}_{gs}$  reaction channel. The vertical dashed lines are shown to illustrate the number of excited levels of  $^{59}\text{Co}$  that are populated up to a particular excitation cutoff, as indicated by the adjacent label.

because of the assumption of an outgoing proton (and  $^{59}\text{Co}$ ) in the  $Q$  value reconstruction. Similarly to extracting the yields for the triton events from  $^6\text{Li}(n, t)$ , the wraparound contribution from  $^{59}\text{Ni}(n, p)$  does not interfere with extracting the  $^{59}\text{Ni}(n, p_0)^{59}\text{Co}_{gs}$  yields. However, the wraparound contribution does form a potential background underneath the events which correspond to populating the excited states of  $^{59}\text{Co}$ .

Lastly, the bottom panel of Fig. 2 shows the detected energy spectrum for the Pt backing target. Here, the strong lines from the positive  $Q$  value reactions are no longer observed, however, the primary background contribution that is observed in all of the targets due to  $^1\text{H}(n, el)$  is present. The other noticeable features in the Pt data are the frame overlap lines due to  $^6\text{Li}(n, t)$  in only one of the detectors. This is due to the fact that all three targets were coloaded on the target ladder in the experimental chamber with the Pt target in the middle, therefore, downscattered low energy neutrons could induce  $(n, t)$  reactions on the off-axis  $^6\text{Li}$  sample and be detected in the silicon detector that was closest to the target ladder. None of these events are observed in the second detector as

the trajectories are shadowed by the first. When the  $^{59}\text{Ni}$  target is in place, the  $^6\text{Li}$  target is moved even further off axis such that these  $(n, t)$  events due to downscattering are no longer a significant source of background.

### C. Pulse-shape selection for particle identification

Variations in the shapes of the detected pulses for different species of incident charged particles can be used for particle identification [28,29] or for the rejection of background events that are not coming from the target position (i.e., reactions from the downstream vacuum chamber window). This pulse shape discrimination (PSD), based on the selection of different rise times, has been used primarily for the discrimination of charged particles over a wide range of mass/charge, well above  $A > 4$ , as discussed in Refs. [29,30]. For our application, we are concerned primarily with the detection of protons and alphas and the threshold for which we can separate these two types of particles from each other. Deuteron and triton contributions due to  $(n, d)$  and  $(n, t)$  are expected to be

negligible due to the  $Q$  value selection and due to the very small cross sections at incident neutron energies below 10 MeV. Therefore, depending on the needs for a particular experiment, the LENZ setup will typically employ either a more traditional  $\Delta E$ - $E$  telescope coincidence configuration, the use of PSD with thicker detectors in singles mode, or a combination of both. In other cases, like in [23], the combination of choice in detector thicknesses, bias voltage, and orientation with respect to the target position did not allow for the use of PSD in the energy range that was selected, so the reaction channels of interest were selected entirely by the known reaction  $Q$  values. For this experiment, the two 1000  $\mu\text{m}$  thick S1 detectors, biased to 160 V (full depletion was achieved at  $\approx 140$  V), were oriented with the junction side facing away from the target. This has the effect of exaggerating the charge collection time associated with the slower charge carrier mobility for incident charged particles, which will have different penetration depths and a difference in “plasma time.” This configuration allowed for the discrimination between protons and alphas above approximately 4 MeV, based on the observed differences in the rise times (i.e., 100–110 ns for  $20 > E_\alpha > 4$  MeV alphas and 70–100 ns for  $12 > E_p > 4$  MeV protons). Although this threshold is fairly high, the combination of PSD with the selection of reaction  $Q$  value, from kinematics reconstruction, is adequate for identifying the reactions of interest. The selection criteria for the PSD was determined offline, since all waveforms were digitized and recorded.

To validate the selection criteria for the pulse shape discrimination, we typically begin with the  $\text{CH}_2$  calibration target, for which a copious amount of protons are produced. In addition, the  $^{59}\text{Ni} + ^6\text{Li}$  target could be used to select alphas, tritons [from  $^6\text{Li}(n, t)^4\text{He}$ ] and protons [from  $^{59}\text{Ni}(n, p)$ ] based on the reaction  $q$  values. The outcome of the PSD selection is highlighted in Fig. 5, showing both the ungated and proton-gated spectra for the  $^{59}\text{Ni}$  target. As the incident neutron energy increases (bottom panel), additional  $^{59}\text{Ni}(n, \alpha)$  reaction channels are open that form a background underneath the isolated  $^{59}\text{Ni}(n, p_0)$   $^{59}\text{Co}_{gs}$  peak that are separated from each other based on the proton PSD selection.

#### D. Background analysis

The primary sources of background in the work are due to  $(n, z)$  reactions on the vacuum window at the entrance and exit to the experimental chamber, on the Pt backing material in the target, and due to the detection of downscattered neutrons in the silicon detectors themselves. The latter creates background lines due to  $^{28}\text{Si}(n, p)^{28}\text{Al}$  and  $^{28}\text{Si}(n, \alpha)^{25}\text{Mg}$  which are observed at incident neutron energies above  $E_n = 5$  MeV, however, these lines do not interfere with the extraction of the  $^{59}\text{Ni}(n, p)$  and  $^{59}\text{Ni}(n, \alpha)$  reaction channels with positive  $Q$  values. As previously mentioned, an additional source of background is attributed to  $^1\text{H}(n, el)$  reactions. These events interfere with the extraction of  $^{59}\text{Ni}(n, p)$  reactions below zero  $Q$  value (corresponding to an excitation energy of approximately 1.85 MeV) in the downstream-most detector. However, due to the rapid variation of outgoing proton energy with respect to the emission angle, these events do not interfere with the extraction of  $(n, p)$  reaction channels below 3 MeV

in excitation energy in the detector closest to the target. Background reactions due to the  $^{nat}\text{Ni}$  content in the target, along with contributions due to low-energy  $^{59}\text{Ni}$  wraparound events, are discussed in Sec. IV.

Lastly, a fairly uniform scattering of uncorrelated background events is observed at all detected energies, as seen in the middle panels of Fig. 2. These events are attributed to LANSCE accelerator dark current, where protons can leak through in between the 1.8  $\mu\text{s}$  micropulse spacing, such that the detected high energy events, corresponding to high incident neutron energies, are not measured at the appropriate prompt time of flight and are distributed uniformly throughout the frame. This LANSCE dark current is monitored and typically kept to an intensity that is  $\ll 0.1\%$  compared to the protons which are delivered at the expected spacing. However, in situations where we use thick targets (e.g., a thin 100  $\mu\text{g}/\text{cm}^2$  sample on a 25  $\mu\text{m}$  thick Pt backing), the increase in background may necessitate a closer monitoring of this dark current than what was traditionally considered acceptable in the past. Regardless, the shape of this background is repeated constantly over the entire frame and can thus be characterized and subtracted.

#### IV. SIMULATION

Past experimental data taken with LENZ, including stable iron, nickel, and brass targets, have been used to validate MCNP [31] and GEANT4 [32] simulations of the LENZ experimental setup. In Ref. [23], we demonstrated the need for improved evaluations of the  $(n, p)$  and  $(n, \alpha)$  reactions on certain stable nuclei, which are used as inputs for MCNP and GEANT4, to accurately predict the experimental backgrounds. Specifically, the need for additional double differential cross section information that incorporate the discrete population of excited states. New evaluations on the outgoing particle spectrum, based on unchanged ENDF/B-VIII.0 reaction cross sections, of  $(n, z)$  reactions for 62 isotopes were performed by Kim *et al.* [33] and are included in our MCNP simulation.

Based on these new evaluations, Fig. 6 shows the expected reaction  $Q$  value spectra for the 95% enriched  $^{59}\text{Ni}$  target, along with contributions due to the stable nickel isotopes. Contributions due to the  $^{60}\text{Ni}$  impurity in the target are negligible, whereas the contributions due to  $^{58}\text{Ni}(n, p)$  result in a reduction of the extracted yield for the excited states populated by  $^{59}\text{Ni}(n, p)$  by approximately 5%. As previously mentioned in Sec. III B, frame overlap contributions due to  $^{59}\text{Ni}(n, p_0)$   $^{59}\text{Co}_{gs}$  at low incident neutron energies will also form a background underneath the events that correspond to populating excited states of  $^{59}\text{Co}$ . The experimental data, at low energies where the cross section is expected to be small for populating the excited states, is used to estimate the scale of the wraparound contribution. The MCNP simulation is then used to determine the background contribution for each of the energy bins and is a small correction ( $<5\%$ ) for incident neutron energies above 2.5 MeV. On the other hand, the excited state yield, which excludes the ground state and is integrated up to a particular excitation energy as discussed in the following section, is reduced by approximately 15% and 30% at 2.15 MeV and 1.55 MeV, respectively, as estimated by

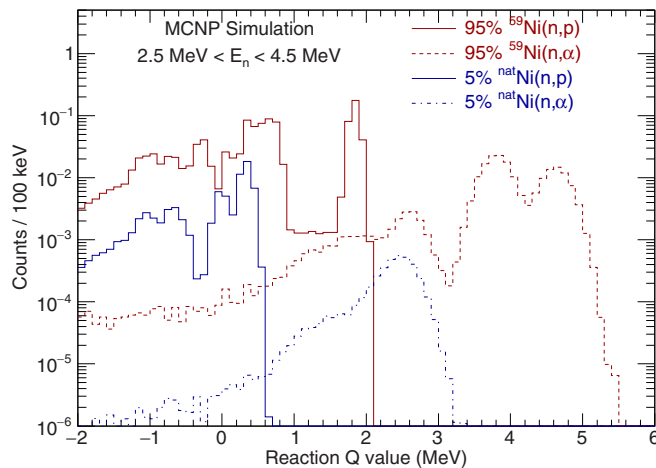


FIG. 6. MCNP simulation of the expected charged particle spectra measured in the upstream-most silicon detector. The simulation has been modified to use an input data library based on the work of Ref. [33], built on ENDF/B-VIII.0 [7], with improved outgoing charged particle spectra that includes the discrete population of the  $(n, p)$  and  $(n, \alpha)$  reactions leading to the ground state and excited states of  $^{59}\text{Co}$  and  $^{56}\text{Fe}$ .

the MCNP simulations. Below 1.5 MeV, the yield is expected to be dominated by the wraparound contributions so excited state yields are not reported below this energy.

## V. RESULTS

The integrated yields for the different reaction channels are obtained for each detector to determine the partial differential cross sections for the  $(n, p)$  and  $(n, \alpha)$  reactions. The angle-integrated partial cross sections, shown in Fig. 7 and Table I, are derived from the yields measured in the detector centered around  $57^\circ$  and by adopting angular distributions based on calculations using a Blatt-Biedenharn formalism, as described in Ref. [33]. The calculated  $(n, p)$  partial differential cross sections show small deviations ( $<5\%$ ) from an isotropic distribution whereas the calculated angular distributions for  $(n, \alpha)$ , although symmetric about  $90^\circ$  in the center of mass, deviate significantly (up to 20% over the entire angle range) from an isotropic distribution. Due to low yields in the forward angle detector, owing to the short run-time of this experiment, we were not sensitive to see these deviations as the results were consistent assuming either an isotropic distribution or the calculated angular distributions between  $20^\circ$  and  $57^\circ$ . In addition, as more partial differential cross sections from populating multiple excited states are summed together, the more the calculated angular distributions are expected to converge to a isotropic distribution. Thus, we base the angle-integrated cross sections on the  $57^\circ$  detector alone which is also more representative of the average differential cross section (assuming either isotropic or the calculation), when weighted by  $\sin \theta$ .

As shown in Fig. 5, the  $^{59}\text{Ni}(n, p_0)$  reaction channel is well isolated from other reaction channels in the  $Q$  value spectra, and the partial cross section for this channel is reported separately from the rest of the  $(n, p)$  partial cross section. In Fig. 7,

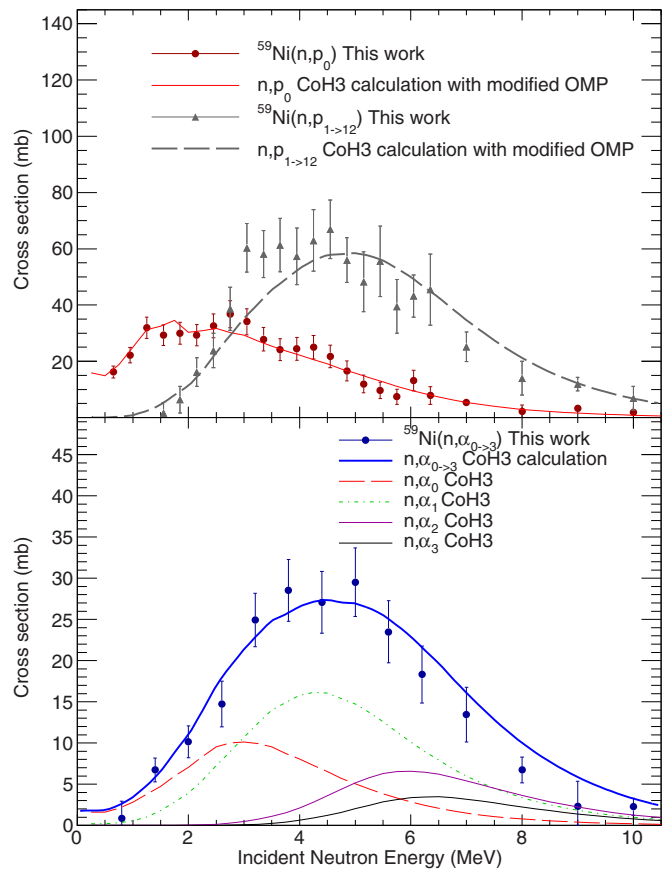


FIG. 7. Top panel: Partial cross section for the  $^{59}\text{Ni}(n, p_0)^{59}\text{Co}_{gs}$  and the summed partial cross section for the excited states, up to an excitation energy of 2.35 MeV. Based on the RIPL database that is used in the calculations, this includes up to the 12th excited state of  $^{59}\text{Co}$ . Bottom panel: The summed partial cross section of the ground state and first three excited states of  $^{56}\text{Fe}$  after being populated by the  $^{59}\text{Ni}(n, \alpha)$  reaction. The cross sections are compared to calculations using CoH<sub>3</sub>, with modified proton optical model and  $^{59}\text{Ni}$  level density parameters.

the  $(n, p)$  partial cross section, excluding the ground state channel and integrating up to an excitation energy in  $^{59}\text{Co}$  of 2.3 MeV, is shown in comparison to  $(n, p_0)$  and in comparison to statistical Hauser-Feshbach calculations using the code CoH<sub>3</sub> [34]. The calculations include modified optical model parameters and  $^{59}\text{Ni}$  level density adjustments, as discussed in the following section. Integrating up to an excitation energy of 2.3 MeV is consistent with summing over the first 12 excited states of  $^{59}\text{Co}$  as given in the RIPL database [35] used in the statistical calculations. Similarly, in the bottom panel of Fig. 7, the  $(n, \alpha)$  partial cross section, summing the ground state and first three excited states in  $^{56}\text{Fe}$ , is shown in comparison to the statistical calculations using CoH<sub>3</sub>. To determine the total  $(n, p)$  and  $(n, \alpha)$  cross sections, the yields are integrated up to a particular cutoff reaction  $Q$  value, corresponding to excitation energies of 4 MeV for  $^{59}\text{Co}$  and 7 MeV for  $^{56}\text{Fe}$ , and a threshold efficiency correction is applied to correct for the yield below this cutoff. This correction is determined using the MCNP simulation of the experimental setup that

TABLE I. Energy- and angle-integrated partial and total cross sections for  $^{59}\text{Ni}(n, p)^{59}\text{Co}$ .

$E_n$	$\sigma_{\pm\text{stat}}^{\pm\text{stat}}_{\pm\text{sys}}$ ( $n, p_0$ )	$\sigma_{\pm\text{stat}}^{\pm\text{stat}}_{\pm\text{sys}}$ ( $1.0 < E_{\text{ex}} < 2.35$ )	$\sigma \pm d\sigma$ ( $n, p_{\text{total}}$ )
0.65	$16.2^{+1.4}_{-1.3}$		$16.7 \pm 2.2$
0.95	$22.2^{+1.7}_{-1.8}$		$23.4 \pm 2.9$
1.25	$31.9^{+2.2}_{-2.6}$		$34.8 \pm 4.1$
1.55	$29.4^{+2.4}_{-2.4}$	$1.7^{+3.7}_{-0.2}$	$30.9 \pm 8.0$
1.85	$30.0^{+2.6}_{-2.4}$	$6.4^{+4.7}_{-0.6}$	$36.4 \pm 9.4$
2.15	$29.3^{+2.6}_{-2.4}$	$16.2^{+4.8}_{-1.5}$	$45.9 \pm 10.0$
2.45	$32.6^{+2.8}_{-2.6}$	$23.9^{+5.7}_{-2.3}$	$58.2 \pm 11.6$
2.75	$36.7^{+3.2}_{-3.0}$	$38.7^{+6.7}_{-3.7}$	$75.0 \pm 15.2$
3.05	$34.1^{+3.3}_{-2.8}$	$60.3^{+6.5}_{-5.8}$	$100.3 \pm 16.8$
3.35	$27.9^{+3.2}_{-2.3}$	$58.1^{+6.3}_{-5.5}$	$97.9 \pm 17.6$
3.65	$24.2^{+3.1}_{-2.0}$	$61.3^{+7.5}_{-5.8}$	$113.2 \pm 18.5$
3.95	$24.4^{+3.3}_{-2.0}$	$57.3^{+8.5}_{-5.5}$	$112.7 \pm 21.1$
4.25	$25.0^{+3.5}_{-2.0}$	$62.9^{+9.1}_{-6.0}$	$137.6 \pm 22.8$
4.55	$21.8^{+3.4}_{-1.8}$	$66.9^{+8.2}_{-6.4}$	$143.2 \pm 24.7$
4.85	$16.6^{+3.2}_{-1.3}$	$56.0^{+5.9}_{-5.3}$	$148.2 \pm 23.6$
5.15	$12.0^{+2.9}_{-1.0}$	$48.3^{+9.6}_{-4.6}$	$134.0 \pm 24.9$
5.45	$9.6^{+2.8}_{-0.8}$	$55.6^{+11.3}_{-5.3}$	$159.6 \pm 26.5$
5.75	$7.4^{+2.6}_{-0.6}$	$39.5^{+8.8}_{-3.8}$	$165.7 \pm 26.9$
6.05	$13.1^{+3.5}_{-1.1}$	$43.2^{+6.2}_{-4.1}$	$196.8 \pm 30.9$
6.35	$7.8^{+3.0}_{-0.6}$	$45.5^{+11.9}_{-4.3}$	$170.5 \pm 35.2$
7.0	$5.4^{+1.1}_{-0.4}$	$25.2^{+4.7}_{-2.4}$	$168.5 \pm 25.1$
8.0	$2.1^{+2.3}_{-0.2}$	$14.0^{+5.9}_{-1.3}$	$172.0 \pm 38.0$
9.0	$3.4^{+1.1}_{-0.3}$	$11.9^{+2.1}_{-1.1}$	$191.3 \pm 55.4$
10.0	$1.8^{+0.9}_{-0.1}$	$6.8^{+4.2}_{-0.7}$	$187.7 \pm 86.1$

incorporates the improved evaluation of Ref. [33] as an input and is based on statistical Hauser-Feshbach calculations. The cross sections, shown in Fig. 8 and Table I, are compared with various evaluations [7–9]. Here, the experimental ( $n, p$ ) cross section data is slightly lower than the available evaluations, in particular at  $E_n < 3$  MeV. Meanwhile, the ( $n, \alpha$ ) cross sections are in fairly good agreement with the available evaluations up to about  $E_n = 5$  MeV. The modifications to the statistical calculations, discussed in the next section, reduce the scale of the calculated ( $n, p$ ) cross section such that it is in good agreement with the experimental data at the lower energies, as was illustrated in Fig. 7.

For the  $^{59}\text{Ni}(n, p_0)^{59}\text{Co}_{\text{gs}}$  partial cross section, the systematic uncertainties in Table I include the uncertainties in the neutron flux normalization (5%), detection efficiency (4%), and number of target atoms (5%). For the partial cross sections that include the excited states of  $^{59}\text{Co}$ , the subtractions to the yield due to  $^{nat}\text{Ni}(n, p)$  is estimated through the MCNP simulation of the experimental setup, assuming an uncertainty of 10% in the scale of the  $^{nat}\text{Ni}$  cross section. The uncertainty in the subtraction of the frame overlap contribution is also derived from the MCNP simulation for each energy bin while the scale of the correction is constrained by the number of counts observed at low incident neutron energy in the exper-

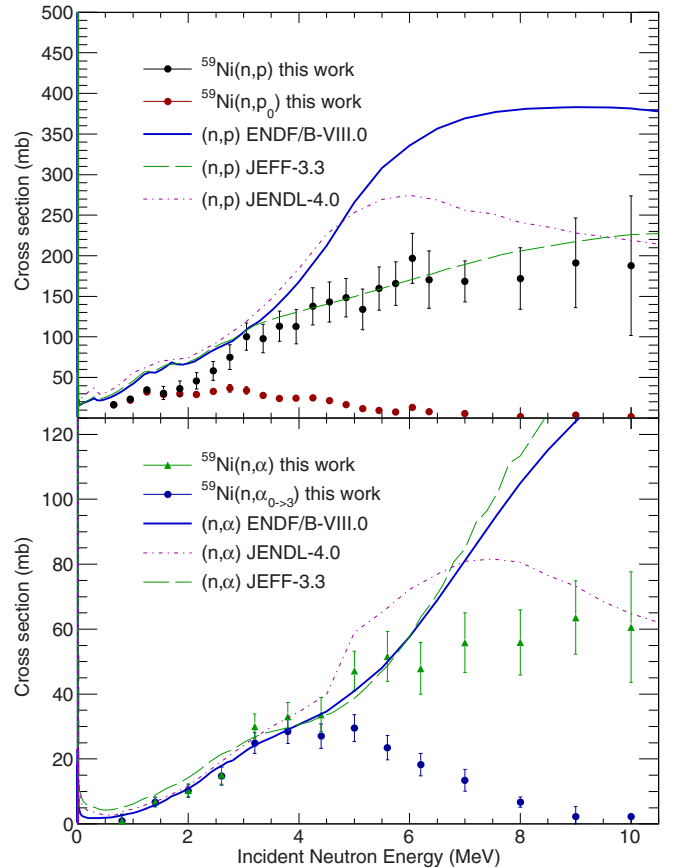


FIG. 8. Integrated ( $n, p$ ) and ( $n, \alpha$ ) reaction cross sections are shown in the top and bottom panels, respectively. The results are shown in comparison to various evaluations [7–9].

imental data. The combination of the two adds an additional 5% to the attributed statistical uncertainty of the ( $n, p$ ) partial cross section [not including the ( $n, p_0$ ) channel] and a similar uncertainty is obtained for  $^{59}\text{Ni}(n, \alpha)^{56}\text{Fe}$ .

## VI. STATISTICAL CALCULATIONS

To further explore the discrepancy between the measured ( $n, p$ ) cross sections and the available evaluations, we perform statistical Hauser-Feshbach calculations using the CoH<sub>3</sub> (version 3.5.4-Miranda) [34] and TALYS1.95 [36] codes. For both the CoH<sub>3</sub> and TALYS calculations, global optical model parameters from Koning and Delaroche [37] are used for the  $n + ^{59}\text{Ni}$  and  $p + ^{59}\text{Co}$  systems and Avrigeanu *et al.* [38] for  $\alpha + ^{56}\text{Fe}$ .

In the ENDF/B-VIII.0 [7] evaluation of  $^{58}\text{Ni}$  and  $^{60}\text{Ni}$ , based on CoH<sub>3</sub> calculations, the surface diffuseness term of the imaginary potential,  $a_w$ , was scaled by a factor of 0.9 for  $n + ^{59}\text{Ni}$  relative to the default parameter to best reproduce the total cross section data. Thus we adopt the same adjustment in the current CoH<sub>3</sub> calculation, although this does not result in a significant change in the overall scale of the ( $n, p$ ) cross section. To bring the calculation into better agreement with both the  $^{59}\text{Ni}(n, p)$  data from this work and the available  $^{59}\text{Co}(p, n)^{59}\text{Ni}$  data from EXFOR, we then adjust the proton



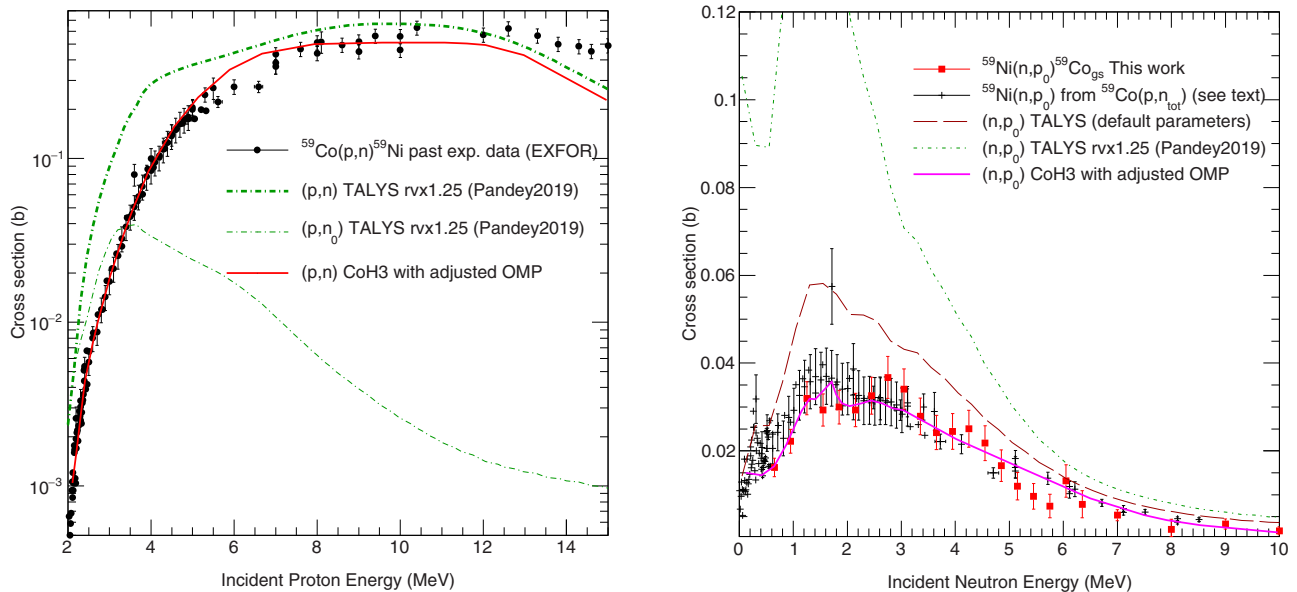


FIG. 9. Left: Past experimental data on the  $^{59}\text{Co}(p, n)^{59}\text{Ni}$  reaction, which is the inverse of the  $^{59}\text{Ni}(n, p)^{59}\text{Co}$  reaction, compared to CoH<sub>3</sub> calculations with modified optical model parameters (see text). The dash-dotted green line shows the calculation (TALYS) using the optical model adjustment suggested by Pandey *et al.* [18] which performs worse in predicting the  $(p, n)$  cross section below 8 MeV than the default parameters. By contrast, adjusting the same parameter in the opposite direction and by a smaller magnitude brings the calculation into better agreement with the  $(p, n)$  data. The calculation that best reproduces the magnitude of the  $(p, n)$  data also better reproduces the magnitude of the  $^{59}\text{Ni}(n, p_0)$  reaction measured in this work (right panel). At incident neutron energies around 2 MeV, the adjustment suggested by Pandey *et al.* leads to calculations that overpredict the measured cross section by a factor of 4–5.

optical model parameters  $a_w$ ,  $r_v$ , and  $r_w$  by modest values of 0.9, 0.95, and 0.95, respectively. This has the effect of reducing the overall scale of the calculated cross section, relative to using the default parameters, for the  $(n, p)$  channel. For  $(n, \alpha)$ , no additional adjustment to the  $\alpha$  optical model parameters was needed to bring the calculation into agreement with the experimental data at low energies. As a consistency check, similar agreement is found when incorporating the same adjustment in TALYS. In addition, to best reproduce the overall trend of the cross sections up to 10 MeV, the  $^{59}\text{Ni}$  level density parameter in CoH<sub>3</sub> was adjusted such that the asymptotic level density parameter,  $a^*$ , was 9.24. For comparison, the  $^{59}\text{Ni}$  asymptotic level density parameter in TALYS, when using the default Gilbert-Cameron level density option, is given as 9.45. CoH<sub>3</sub> has the same level density model, although model parameters are slightly different.

Meanwhile, Pandey *et al.* [18] deduced  $^{59}\text{Ni}(n, xp)$  cross sections using an indirect surrogate ratio method at incident neutron energies above 10 MeV, for which they compared to statistical calculations, based on TALYS, that employed a variety of level density options. To best reproduce the scale and trend of their data, the calculations were modified to use the microscopic level density option from Hilaire's combinatorial tables, and a significant adjustment to the volume radius parameter by a factor of 1.25. By applying the same adjustments to the inverse reaction,  $^{59}\text{Co}(p, n)^{59}\text{Ni}$ , we find that the calculations perform worse in terms of reproducing the overall trend of the available cross section data, as found in the EXFOR [6] database, when compared to using the default parameters. This compares to our adjustment, which involved

a reduction of the volume radius term by a more modest factor of 0.95 to bring the calculation into much better agreement with the  $(p, n)$  data, as shown in Fig. 9 (left), and into better agreement with our  $^{59}\text{Ni}(n, p_0)$  data from this work, as shown in Fig. 9 (right). The adjustment to the statistical calculation, as proposed by Pandey *et al.* based on the surrogate ratio measurement above 10 MeV, results in an  $(n, p_0)$  partial cross section that deviates from our experimental cross section by more than a factor of 4–5 below 2 MeV. In addition, when we calculate the total cross section at 10 MeV we obtain a value of 3.25 barn, which is close to the experimental total cross section for natural Ni. When we increase  $r_v$  by 25%, we get 4.35 barn which is inconsistent with the total cross section data. As an alternative way to compare the  $^{59}\text{Co}(p, n)$  data with our  $^{59}\text{Ni}$  data, we also present data points (shown in black + symbols in the right panel of Fig. 9) that have been inferred from the  $^{59}\text{Co}(p, n)$  cross sections by using the statistical model to determine the ratio of  $(p, n_0)$  to  $(p, n)$  and then using the theorem of detailed balance to convert  $(p, n_0)$  to  $(n, p_0)$ . This approach is relatively insensitive to the choices of optical model parameters and is determined primarily by the partition function that describes the distributions of states and spins in the corresponding nuclei. As expected, both the experimental data from this work and the data inferred from  $(p, n)$  are consistent with the choice of the optical model adjustment that brings the statistical calculation into better agreement with the  $(p, n)$  data. A similar principle is invoked in Ref. [39] as a means to study  $(n, p)$  reactions on unstable nuclei through the study of the inverse  $(p, n)$  reactions. One of the stated goals of this reference is to study the  $^{56}\text{Co}(p, n)^{56}\text{Ni}$

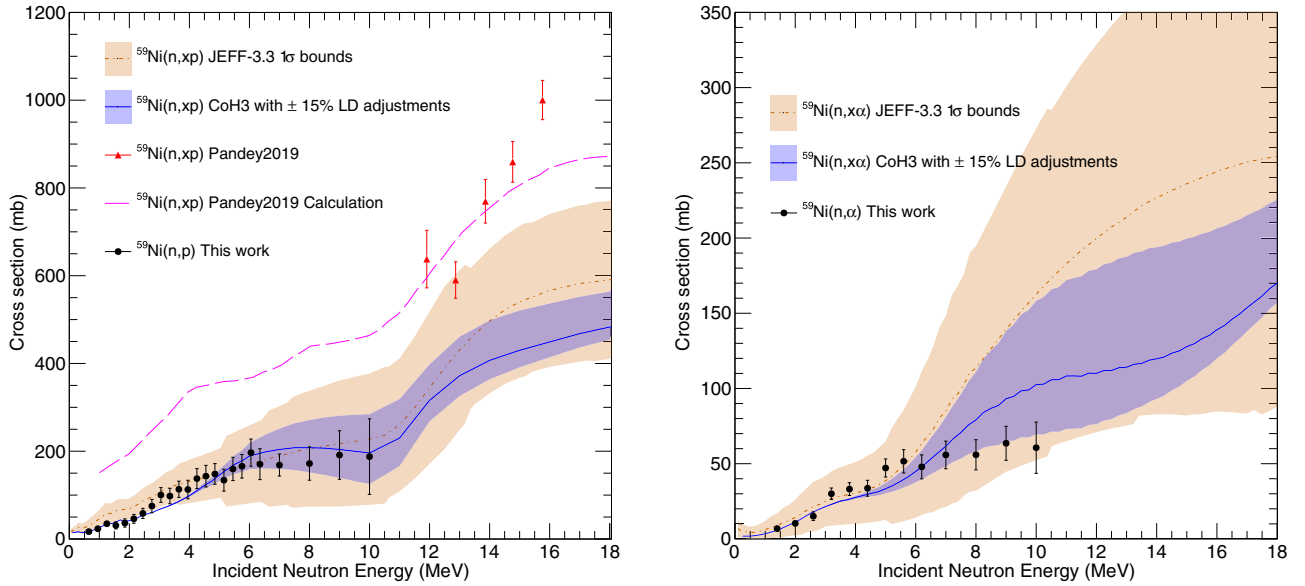


FIG. 10. Comparison of the integrated  $(n, p)$  cross section (left), from this work, with the proton production cross section of Pandey *et al.* [18] that was determined using a surrogate ratio method. The expected energy trend of the calculations, after adjustment to match the magnitude of our experimental data, appears to be significantly inconsistent with the  $(n, xp)$  data. In addition, our results are consistent within the  $1\sigma$  bounds (orange band) of Refs. [9,17], whereas the surrogate work is predominately outside these bounds. The curve labeled “Calculation Pandey2019” is adopted from the curve labeled “TALYS1.8 (enriched)” from Fig. 14 of Ref. [18]. For the  $(n, \alpha)$  comparison (right), the same level density adjustment is shown based on the  $(n, p)$  analysis. Here, no adjustment was made to the default alpha optical model parameters, whereas the proton optical model parameters were adjusted to reproduce the low energy  $(n, p)$  cross sections.

reaction, with a radioactive  $^{56}\text{Co}$  beam, which will provide complimentary information to the direct  $^{56}\text{Ni}(n, p)^{56}\text{Co}$  measurement that has recently been performed at LANSCE, and is being led by a subset of authors from the current work.

Finally, the  $^{59}\text{Ni}(n, p)$  data from this work are compared to the  $^{59}\text{Ni}(n, xp)$  data of Pandey *et al.* in Fig. 10. The expected trend of the  $(n, xp)$  cross section from the statistical calculations, after adjusting the parameters to match the scale and trend of the current  $^{59}\text{Ni}(n, p)$  data, is significantly inconsistent (by more than  $3\sigma$ ) with the work of Pandey *et al.* which raises questions about the application of the surrogate ratio method for this case. The shape of the calculated excitation energy spectrum at higher energies changes by adjusting the level density parameters and the level cutoff for which levels are treated discretely from the RIPL database; however, no options appear to simultaneously reproduce both the scale of our experimental data and that of Pandey *et al.* when modest adjustments are made. Here, the blue band shows the effect from adjusting the level density parameter  $a$  by  $\pm 15\%$ . In this case, our results are consistent with the  $1\sigma$  bounds of the Helgesson work [9,17], whereas only one data point from the Pandey work is consistent. It is clear from this comparison that direct measurements on radioactive nuclei are absolutely necessary, when feasible, to validate and benchmark results from measurements derived from indirect “surrogate” methods. For  $(n, \alpha)$ , no adjustment is made to the  $\alpha$  optical model parameters; however, the calculations reflect the same  $^{59}\text{Ni}$  level density adjustments as the  $(n, p)$  case and are in fairly good agreement over the entire energy range

## VII. CONCLUSIONS AND OUTLOOK

As a long-lived radioisotope of nickel,  $^{59}\text{Ni}$  can be found in significant abundances in fission or fusion reactor environments due to the  $^{58}\text{Ni}(n, \gamma)$  and  $^{60}\text{Ni}(n, 2n)$  pathways. However, as the isotope does not occur naturally, it is more difficult to study than its stable counterparts. In this work, we present measurements of  $(n, p)$  and  $(n, \alpha)$  partial and summed cross sections up to 10 MeV using a thin, electroplated,  $^{59}\text{Ni}$  target that was fabricated and first studied at ORELA in the 1970s. Our results are in fairly good agreement with statistical model calculations; however, a small adjustment was needed to reproduce the slightly reduced  $(n, p)$  cross section that was measured. This adjustment was cross-validated with data available from the inverse reaction,  $^{59}\text{Co}(p, n)^{59}\text{Ni}$ , and found to be consistent. In addition, a past indirect surrogate ratio measurement of  $^{59}\text{Ni}(n, xp)$  was also benchmarked against our direct measurement and was found to be significantly inconsistent based on expected trends from statistical calculations. The results call into question the reliability of the surrogate ratio method for this case, for instance, due to the different open breakup channels between  $^{59}\text{Ni}(n, xp)$  and the reference reaction  $^{60}\text{Ni}(n, xp)$  and the fact that the nuclei under study are significantly lighter in mass than past efforts to apply this surrogate ratio method for actinides. Future measurements with the  $^{59}\text{Ni}$  target at the WNR facility at LANSCE, with an increased beam time and additional detector coverage at backward angles, would allow for the measurement to be extended to higher energies and in direct

comparison with the surrogate measurement. However, the current results elucidate how caution must be applied when interpreting data based on indirect “surrogate” methods, which may not be reliable, and that direct measurements on unstable nuclei are absolutely necessary for testing the predictive capabilities of cross section calculations as they extend away from the line of stability in the nuclear chart.

The  $^{59}\text{Ni}(n, p)$  and  $^{59}\text{Ni}(n, \alpha)$  cross section data presented here and the outgoing charged-particle spectra will also be used to help characterize a  $^{56}\text{Ni}$  target that was produced at the Isotope Production Facility (IPF) and studied at the WNR facility at LANSCE using the hotLENZ experimental setup [26]. This radioactive cocktail target, consisting of the short-lived  $^{56}\text{Ni}$ , small quantities of  $^{57}\text{Ni}$ , and large quantities of  $^{59}\text{Ni}$ , is the first of its kind and will provide the first direct measurement of the  $^{56}\text{Ni}(n, p)^{56}\text{Co}$  reaction cross section. In conjunction with the  $^{59}\text{Ni}(n, p)$  measurement, along with new measurements of  $^{58}\text{Ni}(n, p)$  and  $^{60}\text{Ni}(n, p)$  with LENZ, a more holistic approach to the evaluation of the nickel iso-

topes will be possible that will also include nuclear data on radioactive nuclei.

## ACKNOWLEDGMENTS

This work benefits from the LANSCE accelerator facility and is supported by the U.S. Department of Energy under Contract No. 89233218CNA000001 and by the Laboratory Directed Research and Development program of Los Alamos National Laboratory under Project No. 20180228ER. The nuclear data library evaluation work that was used to improve the MCNP simulations in this work benefited from the collaboration between LANL and the Korean Atomic Energy Research Institute (KAERI) and was supported by the I-NERI program under Contract No. NRF-2020M2A8A1000930. The authors also acknowledge the help of Paul Koehler (LANL) for facilitating reobtaining the  $^{59}\text{Ni}$  targets for use at LANSCE, and in this study, and for providing relevant reports and background information on them.

- 
- [1] R. C. Haight, in *ND2007, International Conference on Nuclear Data for Science and Technology, Nice, April 2007* (EDP Sciences, Les Ulis, France, 2007).
- [2] M. Griffiths, *AECL Nucl. Rev.* **2**, 1 (2013).
- [3] L. R. Greenwood and F. A. Garner, *J. Nucl. Mater.* **233–237**, 1530 (1996).
- [4] L. Luneville and D. Simeone, *EPJ Web Conf.* **115**, 02002 (2016).
- [5] P. W. Lisowski, C. D. Bowman, G. J. Russell, and S. A. Wender, *Nucl. Sci. Eng.* **106**, 208 (1990).
- [6] N. Otuka *et al.*, *Nucl. Data Sheets* **120**, 272 (2014).
- [7] D. A. Brown *et al.*, *Nucl. Data Sheets* **148**, 1 (2018).
- [8] K. Shibata *et al.*, *J. Nucl. Sci. Technol.* **48**, 1 (2011).
- [9] A. J. M. Plompen *et al.*, *Eur. Phys. J. A* **56**, 181 (2020).
- [10] J. A. Harvey, J. Halperin, N. W. Hill, S. Raman, and R. L. Macklin, in *International Conference on the Interactions of Neutrons with Nuclei, Lowell, MA, 1976* (U.S. DOE, Washington, 1976), Vol. 1, p. 143.
- [11] P. Koehler (private communication).
- [12] C. Weiß *et al.*, *Nucl. Data Sheets* **120**, 208 (2014).
- [13] J. McDonald and N. G. Sjostrand, in *Nuclear Cross Sections and Technology, Proceedings of a Conference, Washington, 1975* (National Bureau of Standards, Washington, 1975), p. 810.
- [14] H. M. Eiland and G. J. Kirouac, *Nucl. Sci. Eng.* **53**, 1 (1974).
- [15] S. Raman, E. T. Journey, J. A. Harvey, N. W. Hill, Oak Ridge National Laboratory Report No. 5025, 1975 (unpublished), p. 110.
- [16] W. Hauser and H. Feshbach, *Phys. Rev.* **87**, 366 (1952).
- [17] P. Helgesson, H. Sjöstrand, and D. Rochman, *Nucl. Data Sheets* **145**, 1 (2017).
- [18] J. Pandey, B. Pandey, A. Pal, S. V. Suryanarayana, S. Santra, B. K. Nayak, E. T. Mirgule, A. Saxena, D. Chattopadhyay, A. Kundu, V. V. Desai, A. Parihari, G. Mohanto, D. Sarkar, P. C. Rout, B. Srinivasan, K. Mahata, B. J. Roy, S. De, and H. M. Agrawal, *Phys. Rev. C* **99**, 014611 (2019).
- [19] J. E. Escher, J. T. Harke, F.S. Dietrich, N. D. Scielzo, I. J. Thompson, and W. Younes, *Rev. Mod. Phys.* **84**, 353 (2012).
- [20] S. Chiba and O. Iwamoto, *Phys. Rev. C* **81**, 044604 (2010).
- [21] L. R. Hlondo and B. Lalremruata, *Nucl. Phys. A* **1000**, 121844 (2020).
- [22] H. Y. Lee, S. Mosby, R. C. Haight, and M. C. White, *EPJ Web Conf.* **122**, 05004 (2016).
- [23] S. A. Kuvin, H. Y. Lee, T. Kawano, B. Di Giovine, A. Georgiadou, C. Vermeulen, M. White, L. Zavorka, and H. I. Kim, *Phys. Rev. C* **102**, 024623 (2020).
- [24] <http://www.micronsemiconductor.co.uk/>
- [25] S. A. Wender *et al.*, *Nucl. Instrum. Methods Phys. Res. Sect. A* **336**, 226 (1993).
- [26] B. DiGiovine *et al.*, *Nucl. Instrum. Methods Phys. Res. Sect. A* **1013**, 165631 (2021).
- [27] S. A. Kuvin, H. Y. Lee, B. DiGiovine, A. Georgiadou, S. Mosby, D. Votaw, M. White, and L. Zavorka, *Phys. Rev. C* **104**, 014603 (2021).
- [28] C. A. J. Ammerlaan, R. F. Rumphorst, and L. A. CH. Koerts, *Nucl. Instrum. Methods* **22**, 189 (1963).
- [29] G. Pausch *et al.*, *IEEE Trans. Nucl. Sci.* **43**, 1097 (1996).
- [30] J. Lu *et al.*, *Nucl. Instrum. Methods Phys. Res. Sect. A* **471**, 374 (2001).
- [31] C. J. Werner (ed.), MCNP users manual - code, version 6.2 (2017), [https://mcnp.lanl.gov/mcnp\\_manual.shtml](https://mcnp.lanl.gov/mcnp_manual.shtml).
- [32] S. Agostinelli *et al.*, *Nucl. Instrum. Methods Phys. Res. Sect. A* **506**, 250 (2003).
- [33] H. I. Kim *et al.*, *Nucl. Instrum. Methods Phys. Res. Sect. A* **963**, 163699 (2020).
- [34] T. Kawano, in *Proceedings of the 6th International Workshop on Compound-Nuclear Reactions and Related Topics CNR\*18*, edited by J. Escher, Y. Alhassid, L. A. Bernstein, D. Brown, C. Fröhlich, P. Talou, and W. Younes (Springer, Cham, 2021), Vol. 254, pp. 27–34.
- [35] R. Capote *et al.*, *Nucl. Data Sheets* **110**, 3107 (2009).
- [36] A. J. Koning and D. Rochman, *Nucl. Data Sheets* **113**, 2841 (2012).
- [37] A. J. Koning and J. P. Delaroche, *Nucl. Phys. A* **713**, 231 (2003).
- [38] M. Avrigeanu *et al.*, *At. Data Nucl. Data Tables* **95**, 501 (2009).
- [39] P. Gastis *et al.*, *Nucl. Instrum. Methods Phys. Res. Sect. A* **985**, 164603 (2021).